Monthly Notices of the ROYAL ASTRONOMICAL SOCIETY

MNRAS **458,** 2476–2491 (2016) doi:10.1093/mnras/stw460
Advance Access publication 2016 March 1

Understanding discs in binary YSOs – detailed modelling of VV CrA

P. Scicluna,[1,2⋆] S. Wolf,[1] T. Ratzka,[3] G. Costigan,[4] R. Launhardt,[5] C. Leinert,[5] F. Ober,[1] C. F. Manara[6] and L. Testi[7,8,9]

[1]*ITAP, Universität zu Kiel, Leibnizstr. 15, D-24118 Kiel, Germany*
[2]*Academia Sinica, Institute of Astronomy and Astrophysics, Taipei 10617, Taiwan*
[3]*Institute for Physics/IGAM, NAWI Graz, Karl-Franzens-Universität, Universitätsplatz 5/II, A-8010 Graz, Austria*
[4]*Leiden Observatory, University of Leiden, PB 9513, NL-2300 RA Leiden, the Netherlands*
[5]*Max-Planck-Institut fr Astronomie, Königstuhl 17, D-69117 Heidelberg, Germany*
[6]*Scientific Support Office, Directorate of Science and Robotic Exploration, European Space Research and Technology Centre (ESA/ESTEC), Keplerlaan 1, NL-2201 AZ Noordwijk, the Netherlands*
[7]*European Southern Observatory, Karl-Schwarzschild-Str. 2, D-85748 Garching b. München, Germany*
[8]*Excellence Cluster Universe, Boltzmannstr. 2, D-85748 Garching, Germany*
[9]*INAF – Osservatorio Astrofisico di Arcetri, Largo E. Fermi 5, I-50125 Firenze, Italy*

Accepted 2016 February 24. Received 2016 February 23; in original form 2016 January 24

ABSTRACT

Given that a majority of stars form in multiple systems, in order to fully understand the star- and planet-formation processes we must seek to understand them in multiple stellar systems. With this in mind, we present an analysis of the enigmatic binary T-Tauri system VV Corona Australis, in which both components host discs, but only one is visible at optical wavelengths. We seek to understand the peculiarities of this system by searching for a model for the binary which explains all the available continuum observations of the system. We present new mid-infrared interferometry and near-infrared (NIR) spectroscopy along with archival millimetre-wave observations, which resolve the binary at 1.3 mm for the first time. We compute a grid of pre-main-sequence radiative transfer models and calculate their posterior probabilities given the observed spectral energy distributions and mid-infrared interferometric visibilities of the binary components, beginning with the assumption that the only differences between the two components are their inclination and position angles. Our best-fitting solution corresponds to a relatively low-luminosity T-tauri binary, with each component's disc having a large scaleheight and viewed at moderate inclination ($\sim$50°), with the infrared companion inclined by $\sim$5° more than the primary. Comparing the results of our model to evolutionary models suggests stellar masses $\sim$1.7 $M_\odot$ and an age for the system of 3.5 Myr, towards the upper end of previous estimates. Combining these results with accretion indicators from NIR spectroscopy, we determine an accretion rate of 4.0×10^{-8} $M_\odot$ yr^{-1} for the primary. We suggest that future observations of VV Corona Australis and similar systems should prioritize high angular resolution sub-mm and NIR imaging of the discs and high-resolution optical/NIR spectroscopy of the central stars.

Key words: accretion, accretion discs – protoplanetary discs – binaries: general – stars: pre-main-sequence – stars: variables: T Tauri, Herbig Ae/Be.

1 INTRODUCTION

Stars form in turbulent molecular clouds, and as a result of turbulence, regions of the cloud condense to form cores, which may then continue to collapse under the influence of gravity (e.g. André et al. 2014). This may result in the formation of a single star, or the core may fragment and form many stars (Zinnecker 1984). Angular momentum must be conserved during this collapse, inevitably resulting in any stars being surrounded by a disc of material, which may then be accreted by the star, ejected from the system, or potentially condense into a planetary system (Williams & Cieza 2011). In the event that two or more stars form on gravitationally bound orbits, they will form a binary or multiple protostellar system (Zinnecker 1984).

Protostellar and pre-main-sequence binaries provide unique insights into the star formation process (Zinnecker 1984; Kraus & Hillenbrand 2009; Duchêne & Kraus 2013). Although more complex, it is known that many young stars form as binary or multiple systems. The probability that a companion is present

⋆ E-mail: peterscicluna@asiaa.sinica.edu.tw

depends on the mass of the primary and the environment in which the stars form (for details see Duchêne & Kraus 2013, and references therein). Thanks to their quasi-coeval nature, binary systems provide key tests for models of stellar evolution; pre-main-sequence binaries are therefore crucial to the calibration of evolutionary models at these early stages (Kraus & Hillenbrand 2009). Of particular interest are systems where one or both components still host protoplanetary discs, enabling tests of the evolution of the discs and the star–disc interaction, and in which the binary separation is large, so that the evolution is not complicated by binary interactions (Williams & Cieza 2011). Furthermore, studying coeval systems could yield new constraints for models of planet formation. For example, stars in multiple systems are less likely to be observed to have a disc at any age when compared with single stars (Cieza et al. 2009; Daemgen et al. 2013, 2016), yet planets have been detected in a variety of multiple systems (e.g. Doyle et al. 2011; Roell et al. 2012).

VV Corona Australis (VV CrA) is a young binary system in the Corona Australis star-forming region. Situated approximately 20 arcmin south-east of the prominent Coronet cluster, it is the brightest component in what appears to be a smaller condensation of young stars (Sicilia-Aguilar et al. 2013). Previously thought to be a single star, according to Reipurth & Zinnecker (1993), a companion was discovered approximately 2 arcsec to the north-east of the optical source by Frogel (unpublished) due to a displacement of the near-infrared (NIR) peak from the optical coordinates. At the time, this companion dominated the NIR emission of the system despite being too extinguished to be visible at shorter wavelengths (Chelli, Cruz-Gonzalez & Reipurth 1995). This infrared (IR) companion, now referred to as VV CrA NE, has since faded (Przygodda 2004) such that the optical component (VV CrA SW) is presently the brighter source at all wavelengths at which the binary can be resolved (Kruger et al. 2011). Although the mass ratio of the binary is unknown, throughout this paper we follow Smith et al. (2009) in referring to the optical component VV CrA SW as the primary.

The peculiarities of the binary have made it an intriguing observational target, however it remains enigmatic. The combination of high extinction and ongoing accretion makes the determination of the spectral types of the stars nearly impossible, since veiling fills in many of the photospheric lines (Herczeg & Hillenbrand 2014). Nevertheless, many values have been published for the primary, ranging from K7 (Appenzeller, Jetter & Jankovics 1986) to K1 (Neuhäuser et al. 2000).

Furthermore, the origins of both the high obscuration and the variability of the secondary remain unknown, although two viable solutions have been proposed by Smith et al. (2009). In one solution (their case B) VV CrA NE is inclined such that we view it through its own circumstellar disc, while the second (case A) requires that the disc of the primary is the source of the obscuration. In either case, the variability may be caused either by column density variations leading to changes in the extinction, or by an accretion outburst similar to that of FU Orionis (Smith et al. 2009).

However, some progress has been made thanks to observations across a wide wavelength range. Both sources are variable in the IR, although the variability of the primary is much weaker than that of the secondary. Both show emission in a variety of spectral lines (Prato, Greene & Simon 2003) and appear to be driving outflows (Takami, Bailey & Chrysostomou 2003). Both components are bright in the (sub-)mm, and Lommen et al. (2010) used unresolved Submillimeter Array (SMA) data to determine a total dust mass of 3.9×10^{-4} $M_{\odot}$ for the binary, and a spectral index indicative of significant grain growth.

In this paper, we present a selection of new observations along with a re-reduction of archival data, which are then used, along with data from the literature, to constrain radiative transfer modelling. In Section 2, we present new IR interferometric and spectroscopic data along with archival sub-millimetre observations. Section 3 gives an overview of the methods used for the radiative transfer calculations and to infer the best-fitting model, the results of which are discussed in Section 4. We then discuss observational priorities that will enable future modelling efforts to improve upon our results, before summarizing our conclusions in Section 5.

2 OBSERVATIONS

2.1 MIDI visibilities

VV CrA was observed in 2004 June, 2004 November, and 2005 May (Table 1) with the Mid-infrared Interferometric (MIDI) instrument (Leinert et al. 2003a,b; Morel et al. 2004) at the Very Large Telescope (VLT) Interferometer, as part of programmes ESO-074.C-0209(A) and ESO-075.C-0014(A) (PI Leinert). Both components of the binary were individually measured due to their comparatively large separation. The baselines UT1–UT3, UT2–UT3, and UT3–UT4 were used and the collected light was dispersed with the prism ($R \sim 30$).

The data were reduced with the MIA+EWS package.[1] MIA is based on the analysis of the power spectrum, while EWS implements a coherent analysis of the interferometric fringe signal (Jaffe 2004). The visibilities used for the modelling have been derived with MIA and confirmed with EWS. All visibilities have been calibrated by all the calibrators taken in the same night. The stability of the transfer function is reflected by the errors shown together with the visibilities. Calibrators with peculiar visibilities have been ignored and are indicated in the journal of observations (Table 1).

For technical reasons, the single dish spectra derived from MIDI measurements vary over time in absolute calibration. Therefore, they are scaled to the better calibrated Thermal Infrared Multimode Instrument (TIMMI2) spectra from Przygodda (2004)

We also include three older measurements already obtained with MIDI in 2003 June (Przygodda 2004). These observations have been made with projected baseline lengths between 99.7 and 102.2 m along position angles between 35°.7 and 23°.9.

The resulting visibilities are plotted in Fig. 1. Two observations of VV CrA NE are excluded from the plot and from the model fitting (Section 3); these are flagged in Table 1 as *b*.

2.2 CRIRES spectra

VV CrA SW was observed three times over the nights 2013 August 22–24 as part of programme ESO-091.C-0768(A) (P.I. Costigan) with the Cryogenic high resolution Infrared Echelle Spectrograph (CRIRES) instrument at the European Southern Observatory (ESO)-VLTI (Kaeufl et al. 2004).

The observations were performed with a central reference wavelength of 2170.573 nm and slit width of 0.4 arcsec giving a spectral resolution $R = \frac{\lambda}{\Delta\lambda} \sim 50\,000$. In order to provide good sky subtraction, the star was nodded along the slit between individual exposures. Three sub-integrations of 30 s were taken for each observation. Standard reduction steps for IR observations were performed using IRAF, including flat-fielding, bias-subtraction and spectral extraction. Due to the nodding on the slit, each observation block

[1] http://www.strw.leidenuniv.nl/nevec/MIDI/

Table 1. Journal of MIDI Observations. The length and position angle of the projected baseline has been determined from the fringe tracking sequence, the airmass from the photometric frames.

Date of observation	Universal time	Object	*IRAS* (Jy)	Proj. Baseline (m)	(deg)	AM	Interferometric frames	Photometric frames	Flags
02-06-2004	00:33–00:55	HD 112213	10.8	45.4	40.8	1.1	8000×12 ms	2×1500×12 ms	[a]
02-06-2004	06:59–07:27	VV CrA SW		45.7	42.7	1.0	8000×15 ms	2×1500×15 ms	
02-06-2004	07:33–07:48	HD 178345	8.6	44.9	45.1	1.0	8000×15 ms	2×1500×15 ms	[a]
02-06-2004	07:57–08:40	VV CrA SW		43.0	51.0	1.1	8000×15 ms	2×1500×15 ms	
02-06-2004	10:14–10:31	HD 178345	8.6	35.2	61.3	1.4	8000×15 ms	2×1500×15 ms	[a]
04-11-2004	00:01–00:26	HD 178345	8.6	57.0	145.7	1.4	20000×12 ms	2×5000×12 ms	[a]
04-11-2004	01:07–01:31	VV CrA SW		52.7	164.8	2.0	12000×12 ms	2×3000×12 ms	
04-11-2004	01:31–02:10	VV CrA NE		51.9	175.9	2.6	12000×12 ms	2×3000×12 ms	[b, c]
04-11-2004	02:10–02:47	HD 188603	11.5	45.5	168.6	2.5	16000×12 ms	2×5000×12 ms	[c]
04-11-2004	02:47–03:54	HD 25604	5.1	60.7	117.1	1.7	16000×12 ms	2×5000×12 ms	
04-11-2004	05:04–05:29	HD 20644	14.7	59.1	101.5	1.7	12000×12 ms	2×3000×12 ms	
04-11-2004	07:18–07:36	HD 37160	6.5	61.0	107.4	1.2	8000×12 ms	2×2000×12 ms	[a]
04-11-2004	09:00–09:23	HD 50778	17.3	61.0	112.6	1.0	8000×12 ms	2×2000×12 ms	
29-05-2005	06:19–07:00	HD 139127	12.3	82.8	51.6	1.3	8000×18 ms	2×4000×18 ms	[d, a]
29-05-2005	07:28–07:56	HD 142198	6.3	92.0	41.8	1.6	8000×18 ms	2×4000×18 ms	
29-05-2005	08:54–09:17	HD 152820	7.6	77.7	49.7	1.7	8000×18 ms	2×4000×18 ms	
29-05-2005	09:17–09:56	VV CrA NE		88.8	47.5	1.2	8000×18 ms	2×4000×18 ms	
29-05-2005	09:56–10:19	VV CrA SW		85.7	49.1	1.3	8000×18 ms	2×4000×18 ms	
29-05-2005	10:19–10:53	HD 178345	8.6	81.6	51.4	1.4	8000×18 ms	2×4000×18 ms	[d, a]
30-05-2005	22:35–23:15	HD 102839	5.9	58.9	91.6	1.4	8000×18 ms	2×4000×18 ms	
30-05-2005	00:17–00:41	HD 102461	8.6	62.0	114.0	1.2	8000×18 ms	2×4000×18 ms	[a, c]
30-05-2005	01:24–01:56	HD 139127	12.3	54.1	88.7	1.2	8000×18 ms	2×4000×18 ms	[d, a]
30-05-2005	01:56–02:09	HD 139127	12.3	56.1	92.1	1.1	8000×18 ms	2×4000×18 ms	[e, a, c]
30-05-2005	03:18–03:45	HD 178345	8.6	41.6	73.1	1.5	8000×18 ms	2×4000×18 ms	[a]
30-05-2005	03:45–03:58	HD 178345	8.6	43.5	75.9	1.4	8000×18 ms	2×4000×18 ms	[e, a]
30-05-2005	03:58–04:29	VV CrA NE		48.7	84.8	1.3	8000×18 ms	2×4000×18 ms	
30-05-2005	04:29–04:42	VV CrA NE		50.4	87.0	1.2	8000×18 ms	2×4000×18 ms	[e, b]
30-05-2005	04:42–05:04	VV CrA SW		53.0	90.3	1.2	8000×18 ms	2×4000×18 ms	
30-05-2005	05:04–05:16	VV CrA SW		54.4	92.1	1.1	8000×18 ms	2×4000×18 ms	[e]
30-05-2005	05:16–05:28	VV CrA SW		55.7	93.9	1.1	8000×18 ms	2×4000×18 ms	[e]
30-05-2005	05:28–05:49	VV CrA NE		57.6	96.9	1.1	8000×18 ms	2×4000×18 ms	
30-05-2005	05:49–06:14	HD 133774	8.4	49.4	130.6	1.3	8000×18 ms	2×4000×18 ms	[a]
30-05-2005	07:01–07:35	HD 139127	12.3	57.6	149.7	1.5	8000×18 ms	2×4000×18 ms	[d, a]
30-05-2005	08:08–08:31	HD 152820	7.6	54.5	144.1	1.4	8000×18 ms	2×4000×18 ms	
30-05-2005	08:55–09:21	HD 164064	5.0	42.2	124.9	1.5	8000×18 ms	2×4000×18 ms	
30-05-2005	09:21–10:26	VV CrA NE		56.7	142.8	1.3	8000×18 ms	2×4000×18 ms	
30-05-2005	10:26–10:59	HD 178345	8.6	56.7	147.2	1.5	8000×18 ms	2×4000×18 ms	[d, a, c]

[a] spectrophotometric calibrator;
[b] excluded from fitting;
[c] peculiar instrumental visibility;
[d] photometry of one or both beams repeated;
[e] no recentering of the beams performed.

results in two spectra which were then median combined. These spectra were then telluric corrected with standards observed on the night.

The wavelength range covered by these observations is ∼ 2143–2195 nm. Unfortunately, there were no photospheric lines visible within these spectra, and so a spectral type derivation was not possible. However, the Br γ emission line lies within this range, and is closely associated with accretion (Muzerolle, Hartmann & Calvet 1998; Calvet et al. 2004; Antoniucci et al. 2011). No significant variations in the equivalent width (EW) of this line were measured over the course of the three nights (see Fig. 2), with a mean measurement of 9 ± 0.7 Å.

Using the observed Near Infrared Camera (NIRC) *K*-band flux of 1.63 Jy for this target (Koresko, private communication), corrected for extinction using the redding law by Steenman & The (1991), we converted the Br γ EW into a luminosity (taking the distance to VV CrA SW to be 130 pc; Marraco & Rydgren 1981) which was found to be 7.2×10^{-4} $L_{\odot}$. Using the Alcalá et al. (2014) accretion luminosity relation for Br γ, this then gives an accretion luminosity of 0.81 ± 0.07 $L_{\odot}$. Here, the spread comes from considering the spread in the measured EW over the course of the three days.

Following the methods of Sanchez-Bermudez et al. (2014), we also tested for the presence of any extended emission from the Br γ line using spectro-astrometry. The original observations were not designed to probe the surrounding structure, and so only contained one position angle. The only conclusion we can so derive from these observations is that there is no signal of extended emission at the 1–10 mas level in the Br γ line in the north–south direction.

2.3 Millimetre continuum data

2.3.1 SMA data

In order to improve the constraints on the emission at long wavelengths, we retrieved archival data taken using the Submillimetre

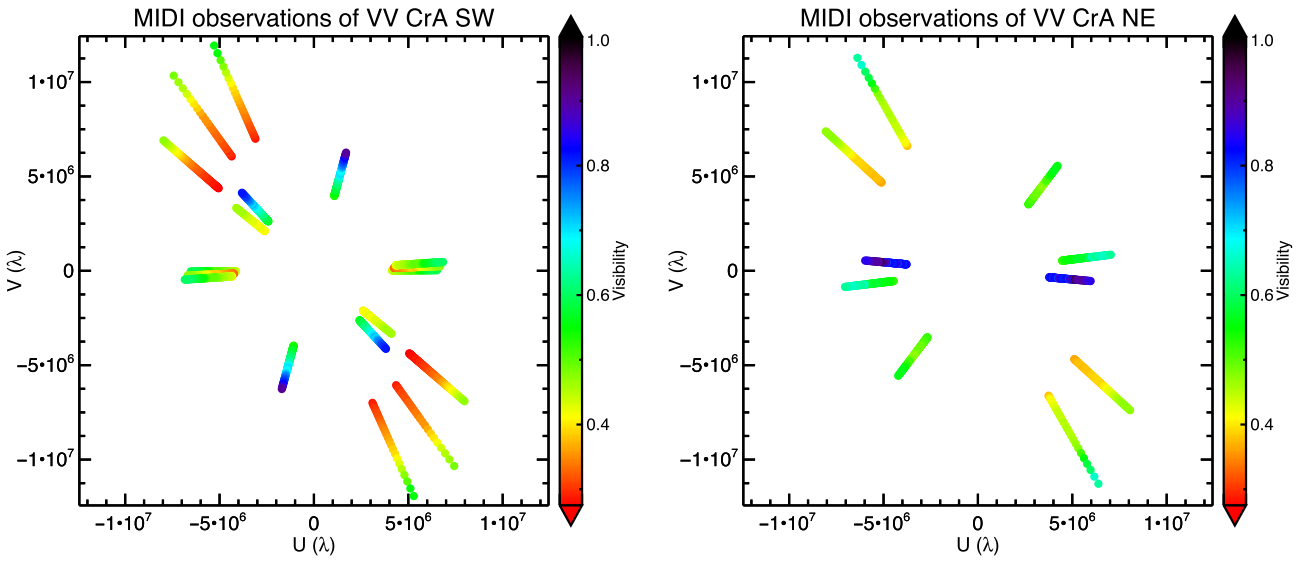

(a) (b)

Figure 1. (a) Wavelength-resolved visibilities plotted in the UV plane for the observations of VV CrA SW. (b) As (a) but for the five observations of VV CrA NE. UV distances are shown in units of the wavelength; as a result, each line has the longest wavelengths towards the centre and shortest wavelengths towards the edge of the plot.

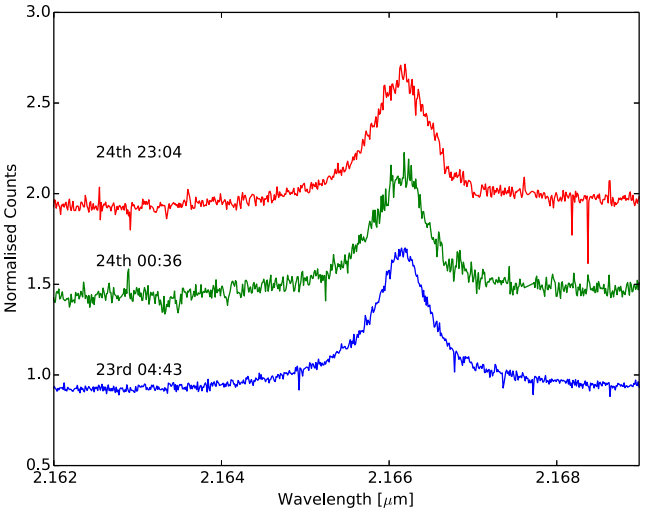

Figure 2. Median-combined CRIRES spectra from each observing night, showing the region of the spectra covering the Br γ line.

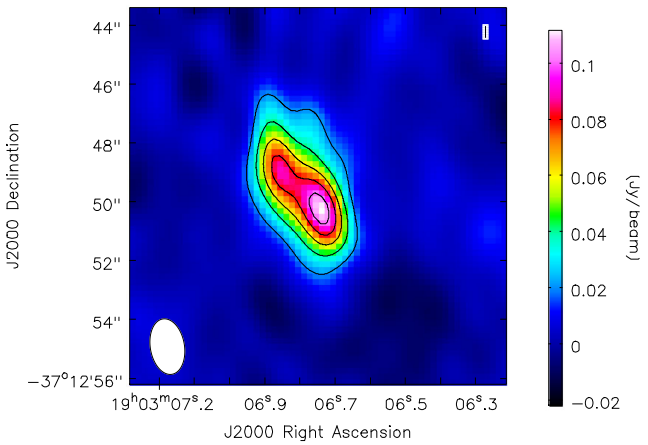

Figure 3. Final reduced continuum image reconstructed from the SMA observations at 1.3 mm. The white oval shows the size and shape of the synthesized beam.

Array at 1.3 mm. VV CrA was observed on 2008 October 01 in Compact configuration with six antennas (previously published in Lommen et al. 2010) and on 2012 September 12 and 18 in extended configuration with seven antennas (unpublished). Both data sets were reduced separately and in combination to explore the loss of flux on large scales.

The calibrated data was downloaded from the SMA archive and imaged using CASA. After masking edge channels and checking for the presence of spectral lines, the data were imaged interactively using the *clean* routine with natural weighting. The final reduced image, using both array configurations, is shown in Fig. 3. Clearly resolved peaks are visible at approximately the same positions as the IR locations of the two sources. In order to extract continuum fluxes, 2D Gaussians were fitted simultaneously to both components using the IMFIT routine with the literature positions of the two components as initial guesses. Images reconstructed using only the extended array observations resolve both components of the binary more clearly, separating the two peaks more distinctly, however more than 50 per cent of the single-dish flux detected by Chini et al. (2003) is missing. We therefore do not show the image or use it to derive fluxes. Folding in the observations taken in the compact configuration reduces this missing-flux problem somewhat, although there is still ∼25 per cent missing flux. This suggests that either circumbinary structure or structure associated with the parent cloud are being filtered out; future observations using ALMA including the compact array are required to identify the source of this emission.

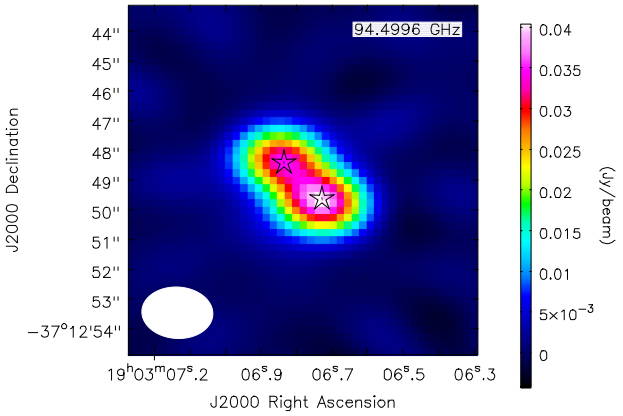

Figure 4. Reconstructed image from the 2005 ATCA data set. The approximate locations of the two components are marked by stars.

2.3.2 ATCA observations

Prior to the 2008 observations presented by Lommen et al. (2010), VV CrA was observed with the Australia Telescope Compact Array (ATCA) at 3 mm on 2005-08-14 in configuration H75 and on 2005-08-17 in H214, with good weather conditions for both observations. Combining the two configurations provided physical baselines ranging from 22 to 247 m. All antennas were equipped with cooled superconductor-insulator-superconductor (SIS) receivers, which provided average system temperatures of 200–350 K at the observing frequency. A digital correlator was used with two 128 MHz wide spectral windows centred at 93.504 and 95.552 GHz, respectively. Combining the two sidebands resulted in an effective observing wavelength of 3.17 mm. The primary beam size at this wavelength was $\sim$ 38 arcsec. Amplitude and phase were calibrated through frequent observations (typically every 20 min) of the nearby quasar 1921–293. The absolute flux density was calibrated using the secondary calibrator 1253–055 in each track, the flux of which was regularly compared to Uranus and adopted as 14.7 Jy for the time of the observations. Additional effort was made to improve the gain-elevation calibration of the antennas, which can significantly affect the flux-density scale, especially when observing at high elevation. The resulting total flux uncertainty is estimated to be $\sim$ 20 per cent.

The data were calibrated and images produced from the combined UV data using MIRIAD (Sault, Teuben & Wright 1995) and its CLEAN algorithm. Of the different UV-weighting schemes explored, the image produced with *robust* UV-weighting parameter −0.5 (Briggs, Schwab & Sramek 1999) was finally selected as the optimum. The resulting synthesized full width at half-maximum beam size is 2.39 arcsec × 1.73 arcsec (PA 86.°7). The 1σ noise level in the final map is $\sim$ 1 mJy beam^{-1}.

The resulting image (Fig. 4) clearly resolves the two sources, although the individual sources (discs) remain unresolved and separating disc emission from possible envelope or circumbinary contributions is not feasible. Image plane fitting of 2D Gaussians results in integrated fluxes of 40 ± 8 and 35 ± 8 mJy for the SW and NE components, respectively. The total flux density of 75 ± 15 mJy was consistently measured from both the UV data and the image plane. This value is consistent with the total flux of 69.5 ± 14 mJy (at the same frequency) reported by Lommen et al. (2010) from their measurements on 2008-08-02, although the fluxes they attribute to the individual components are about 25 per cent lower than ours (albeit with similar flux ratio). These slight discrepancies between individual contributions and total flux could both be a result of their missing short baselines (H214 config only) or our uncertainties in separating disc from extended emission. However, Lommen et al. (2010) report for 2008-08-03, i.e. only one day later, a total flux density of only 44.2 ± 9 mJy. Although we cannot exclude that this points to a real short-term flux variability, the consistency between their 2008-08-02 flux and our 2005 flux makes this unlikely.

The 3 mm fluxes are not included in our subsequent model fitting for a number of reasons. First and foremost, it is not possible to uniquely attribute the differences between our fluxes and the Lommen et al. (2010) fluxes to either measurement uncertainty or real variability. Secondly, as discussed below, we cannot exclude a significant contribution from free–free emission at 3 mm, while the model only treats dust emission.

Using these new resolved 1.3 and 3 mm fluxes, we derive spectral indices $\alpha_{\rm mm}$ of 1.9 ± 0.4 and 1.8 ± 0.4 for the primary and secondary, respectively. These can be compared with values of $\alpha_{\rm mm}$ of 2.2 ± 0.5 and 2.3 ± 0.6 when using our 1.3 mm fluxes and the Lommen et al. (2010) 3 mm fluxes; both values are mutually consistent as expected. This indicates either substantial grain-growth, with a sizeable population of grains with radius > 1 mm, that the discs are very optically thick at mm-wavelengths, or a significant contribution from free–free emission at 3 mm. However, further observations are required to attribute this to a particular mechanism.

3 MODELLING

3.1 Radiative transfer modelling with MC3D

MC3D (Wolf, Henning & Stecklum 1999; Wolf 2003) solves the radiative transfer (RT) equation self-consistently using Monte Carlo (MC) methods. Optimized for dusty circumstellar discs, it randomly propagates packets of radiative energy (photons) through the medium. Each packet is monochromatic and of fixed energy. Packets interact randomly with the medium, either through scattering events – in which only the direction and stokes vector of the photon change – or absorption & re-emission events – where the wavelength of the re-emitted photon is likely to change. For a given dust-density distribution, MC3D calculates the temperature distribution, and scattered and re-emitted fluxes.

The temperature distribution is calculated assuming that the dust is in local thermodynamical equilibrium and that the dust is heated only by the central star. Once the dust-temperature distribution has been calculated, the spectrum of thermal re-emission can be calculated. For computational efficiency, this is done using ray-tracing techniques. Rays are generated ensuring that they sample all cells in the grid, stepped through the model grid to integrate the flux along each line of sight, and projected on to a detector. As this method only considers the contribution of thermal emission by dust, we also compute the contribution of the stellar radiation and scattered flux through monochromatic radiative transfer, in which the star launches radiation packets at each wavelength of interest, which are followed until they exit the model space. Images are computed using the same methods, with the results resolved into a number of pixels.

3.1.1 Disc density distribution

Although the radiative transfer is performed in three dimensions, to reduce the computational time we consider only 2D, axisymmetric disc density distributions, which take the form

$$\rho\left(R,z\right)=\rho_0\left(\frac{R}{R_0}\right)^{-\alpha}\exp\left(-\frac{1}{2}\left(\frac{z}{h\left(R\right)}\right)^2\right), \quad (1)$$

where the scaleheight h is given by

$$h(R) = h_0 \left(\frac{R}{R_0} \right)^{\beta}, \quad (2)$$

where $R_0 = 100$ au, based on the α-viscosity disc of Shakura & Sunyaev (1973). The above density distribution is defined in the range $R_{\rm in} \leq R \leq R_{\rm out}$, the inner and outer radii of the disc. For a vertically isothermal gaseous disc in hydrostatic equilibrium $\alpha = 3(\beta - 0.5)$ (Shakura & Sunyaev 1973); given that we only treat small grains (see Section 3.1.2) which should be dynamically coupled to the gas, we opt to define our density distribution only in terms of β. This implicitly assumes that the disc is in hydrostatic equilibrium, although we *do not* compute the equilibrium structure of the disc. This distribution is then normalized to yield the desired total dust mass $M_{\rm d}$. The disc is heated by a star whose spectrum is that of a blackbody $B(T_*)$ scaled to contain the required total stellar luminosity L_*. The temperature only has a significant effect on the emergent flux at optical wavelengths, because the IR emission is determined by the energy balance of the dust, which is dominated by the input luminosity. Similarly, we do not include any accretion luminosity or UV excess, as the optical and UV coverage of the spectral energy distributions (SEDs) are too sparse to be able to constrain this. This approach has been successfully applied in a number of studies of protoplanetary discs, for example Sauter et al. (2009), Madlener et al. (2012), and Gräfe et al. (2013).

3.1.2 *Dust model*

Although there are signs of grain-growth in millimetre-wave observations of VV CrA (Lommen et al. 2010 and Section 2.3) only interstellar medium (ISM)-like dust grains are included in the models. The energy balance of the disc is primarily determined by the more numerous small grains which absorb the stellar radiation more efficiently (Testi et al. 2014). These grains therefore dominate the short-wavelength emission (and hence the MIDI observations) and the total energy absorbed by dust; this in turn determines the integrated energy of the SED. However, large ($\sim$1 mm) grains emit more efficiently at mm wavelengths, and therefore dominate the appearance of (sub-)mm images and the spectral index.

Theoretically, one expects that these larger dust grains should decouple from the gas density distribution, settling towards the midplane of the disc, while gas-drag would cause them to drift towards the inner regions of the disc (Dullemond & Dominik 2004). In the absence of multiwavelength, spatially resolved observations at millimetre wavelengths it is impossible to quantify the distribution of these larger dust grains.

Since the MIDI observations are sensitive only to the surface layers of the inner regions of the disc, which are expected to be populated by smaller grains, only grains with sizes between 5 and 250 nm are included with a power-law size distribution ($q = -3.5$) as in Mathis, Rumpl & Nordsieck (1977), consisting of 62.5 per cent amorphous silicates and 37.5 per cent graphite, using optical constants from Weingartner & Draine (2001), and are assumed to be compact spheres. The cross-sections are computed using Mie calculus and averaged over the size distribution and dust compositions.

3.2 The fitting process

We seek to find a suitable fit by first building a data base of $\sim$1.5 $\times$ 10^6 single-star+disc models, the parameter space for which is shown in Table 2. These models cover a range based on previous literature investigations of the system where possible (e.g. L_*, T_*, $M_{\rm d}$) and a physically motivated range for the others.

Table 2. Parameter space covered by RT models.

Parameter	Range	Step	Prior
D (pc)	130	Fixed	
L_* ($L_\odot$)	4–30	$\times$ 1.16	Flat
T_* (K)	4000–5500	500	Flat
$M_{\rm d}$ ($M_\odot$)	$10^{-4.5}$–10^{-3}	$\times$ $10^{0.5}$	Flat
$R_{\rm in}$ (au)	0.3–1.5	0.2	Flat
$R_{\rm out}$ (au)	200	Fixed	
h_{100} (au)	10–35	5	Flat
β	1.0–1.3	0.05	Flat
i ($^\circ$)	5–85	$\geq 2^\circ$	$\sin i$
A_V (mag)	0.1–1.5	0.2	$HN(\sigma = 0.3)$

For each of these models, MC3D returns output in the form of an SED from 0.3 to 3000 μm and images covering the wavelength range of the MIDI observations. From each image, synthetic interferometric visibilities corresponding to the baselines used in the MIDI observations are calculated using fast Fourier transforms (Haniff 2007). The real and imaginary parts of the synthetic visibilities are determined by linear interpolation between adjacent values in the Fourier plane.

To build models of the binary system, we combine pairs of models and compare the output to the MIDI visibilities and the SED of the system and its components. The fluxes used for the SED are given in Table 3; where possible, we select the most recent and robust photometry available. For each pair of models, we sum the fluxes at wavelengths where no observations are available which resolve the binary in order to robustly include the far-IR (FIR) observations, while the resolved fluxes are compared to the respective member of the model pair. Due to the convergence of the resolved SEDs towards longer wavelengths through *N* and *Q* bands, and the similarity of the SMA fluxes, we consider a subset of binary configurations such that the two components differ only in inclination and position angles, and in which the NE component is obscured by its own disc.

These simulated data are then used to calculate posterior-probability distributions and their marginal distributions for representative binary configurations under certain assumptions. A detailed description of these calculations is given in Appendix A. The likelihood for each datum is calculated using equation (A2), and no additional weighting is applied to the data beyond that implied by their uncertainties and bandwidth, treating photometry and interferometry identically. As a result, our fitting process is naturally most sensitive to the most precise data which integrate over the narrowest wavelength range, which is in general those between 7–13 μm. The product of the likelihoods of all the data for a given model is then inserted into equation (A1) along with the product of the priors of the model (see Table 2) to give the posterior. The best-fitting model is the pair of single-star models which maximises the posterior. It is worth emphasizing that any conclusions drawn in this way are valid only within the parameter space we consider.

4 DISCUSSION

4.1 Best-fitting model and degeneracy

Table 4 lists the parameters of the best-fitting model, and Fig. 5 shows a corner plot of the marginalized posterior distributions, illustrating degeneracies between different input parameters. In particular, $R_{\rm in}$ is degenerate with the inclinations of both discs. These

Table 3. Data used for SED fitting.

Effective wavelength[a] (μm)	Flux (Jy)			Ref.
	SW	NE	Unres	
0.36 ± 0.025	0.0042 ± 0.00014	$< 8\times 10^{-5}$ [b]	**	1,2
0.43 ± 0.036	0.0081 ± 0.00067	< 0.00016 [b]	**	1,2
0.55 ± 0.038	0.0217 ± 0.0008	< 0.0004 [b]	**	1,2
0.7 ± 0.081	0.0510 ± 0.0007	< 0.001 [b]	**	1,2
0.9 ± 0.097	0.117 ± 0.003	< 0.002 [b]	**	1,2
1.25 ± 0.09	0.40 ± 0.06	0.014 ± 0.0098	**	3
1.65 ± 0.12	0.94 ± 0.13	0.153 ± 0.0211	**	3
2.16± 0.13	1.63 ± 0.23	0.846 ± 0.117	**	3
3.8 ± 0.22	1.88 ± 0.35	1.69 ± 0.311	**	3
4.80 ± 0.2	3.50 ± 0.65	2.6 ± 0.47	**	4
7.73 ± 0.245	13.7 ± 0.7	7.0 ± 0.4	**	2
8.74 ± 0.269	14.4 ± 0.2	4.5 ± 0.1	**	2
10.35 ± 0.357	15.0 ± 0.3	3.3 ± 0.1	**	2
12.33 ± 0.415	20.5 ± 0.7	8.7 ± 0.3	**	2
18.3 ± 0.527	28.4 ± 1.6	11.1 ± 0.8	**	2
24.56 ± 0.699	35 ± 18	25.1 ± 13.5	**	2
70 ± 8.84	**	**	55 ± 6	5
100 ± 14.3	**	**	80 ± 12	5
160 ± 31.4	**	**	66 ± 13	5
450 ± 16.8	**	**	12 ± 4	6
850 ± 27.7	**	**	2.0 ± 0.2	6
870 ± 54.2	**	**	1.66 ± 0.06	7
1200 ± 164	**	**	0.58 ± 0.06	8
1270 ± 117	**	**	0.469 ± 0.021	9
1340 ± 22	0.1999 ± 0.0074	0.1701 ± 0.0083	**	10

[a]Defined as the central wavelength of the filter ± half of the smallest interval, symmetrical about the central wavelength, that contains at least 68.3 per cent of the area under the transmission curve.
[b] 3σ upper limits.
References: (1) Marraco & Rydgren (1981); (2) Kruger et al. (2011) ; (3) Koresko (priv. comm.) ; (4) Ratzka et al. (2008) ; (5) Sicilia-Aguilar et al. (2013); (6) Nutter, Ward-Thompson & André (2005); (7) Sicilia-Aguilar et al. (2011); (8) Henning et al. (1994); (9) Chini et al. (2003); (10) this work.

Table 4. Best-fitting model parameters.

Parameter	Best Fit
L_* ($L_\odot$)	4.9
T_* (K)	5500
M_d ($M_\odot$)	10^{-3}
R_{in} (au)	1.3
R_{out} (au)	200
h_{100} (au)	20
β	1.00
i_{SW} (°)	49
i_{NE} (°)	55
A_V (mag)	0.5
PA (SW) (°)[a]	−10
PA (NE) (°)[a]	−50

[a]position angle east of north of the *minor* axis of the disc

are bimodal, with models with smaller $R_{in} \sim 0.3$ preferring solutions with inclinations ∼40°–45° rather than the ∼50°–55° solution of our best-fitting model. Otherwise, parameters are typically constrained to a small region near the value of the best-fitting model, or are upper or lower limits. Unfortunately, the grid resolution is not high enough to determine uncertainties from the marginalized distributions, however it is possible to derive certain robust constraints from Fig. 5. Our results indicate that models with relatively low-luminosity stars with massive, unflared, geometrically thick discs seen at intermediate inclinations are strongly preferred, while the stellar effective temperature and disc position angles are poorly constrained. The luminosity is lower than suggested by some previous models (e.g. Wilking et al. 1992). This is a result of the extreme NIR variability of the NE component, whose *K*-band flux has varied by two orders of magnitude over the last three decades (Kruger et al. 2011).

The SED of the best-fitting model is shown in Fig. 6. Our best-fitting model reproduces the fluxes at short wavelengths ($\lambda \leq 30$ μm) well, although the *JHK*-bands are underpredicted. However, despite the very high dust mass, it does not reproduce the FIR–sub-mm fluxes. The grid does not include higher dust masses because, assuming a typical gas-to-dust ratio of ∼100, the mass of the disc would then be comparable to that of the central object and self-gravity would begin to play a role (Lodato & Rice 2004, 2005), and hence equation (1) would no longer adequately describe the density distribution. This cut-off coincides with an empirical upper limit to dust masses derived from sub-mm observations (Mohanty et al. 2013). Furthermore, the total dust mass of the binary implied by our model (2×10^{-3} $M_\odot$) is five times larger than that determined by Lommen et al. (2010). As a result, further increases to the dust mass would not provide an acceptable solution.

Alternatively, increasing the maximum grain size would increase the sub-mm opacities, and hence increase the emergent flux at these wavelengths. This is demonstrated in Fig. 7, which shows the effect on the SED of increasing the maximum grain size in steps of 1 dex from 0.25 to 250 μm. Increasing the maximum grain size leads to a significant increase in the emission at long wavelengths, and only begins to affect the quality of the fit in the mid-infrared (MIR)

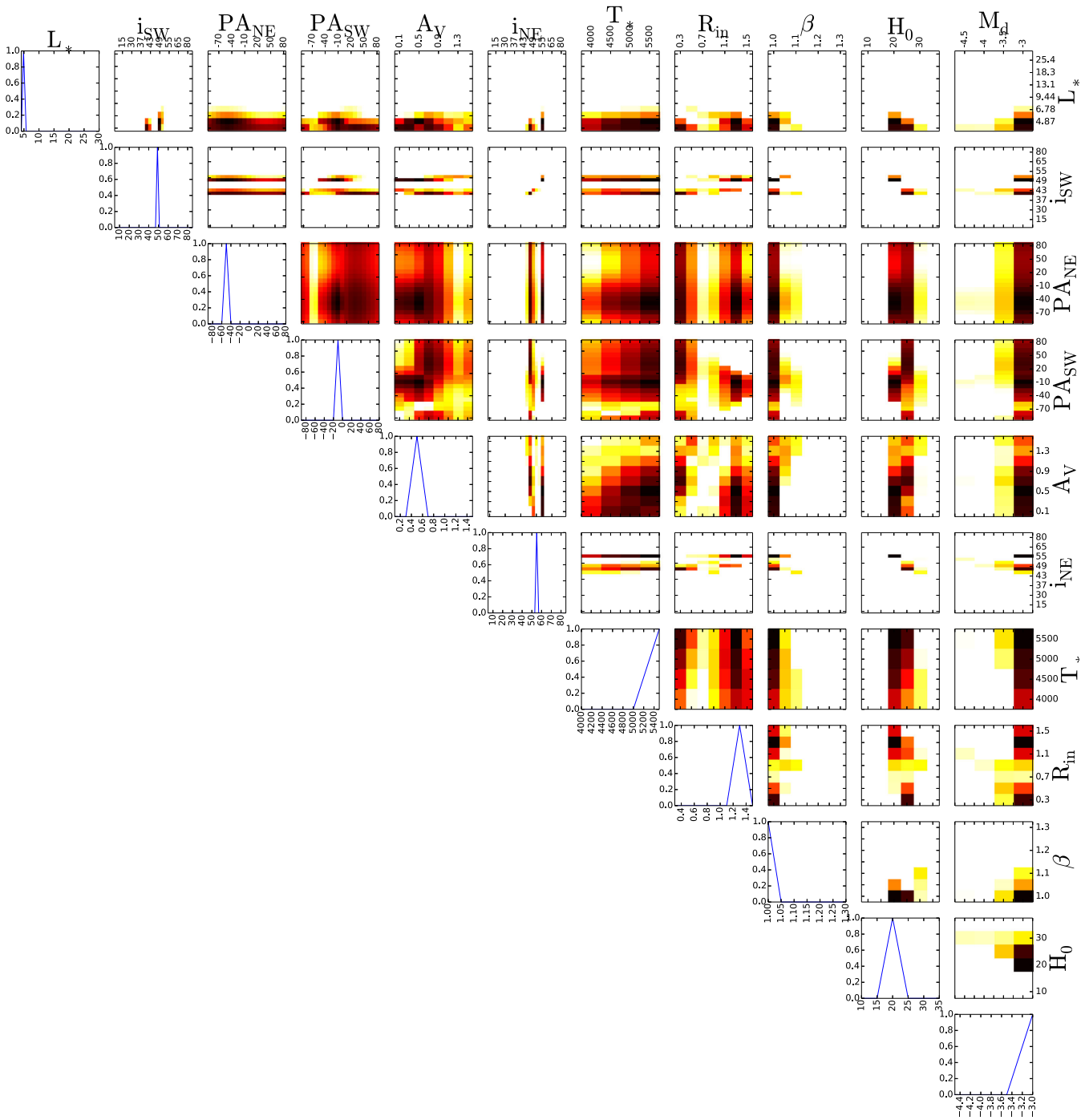

Figure 5. Cornerplot showing the degeneracies between the various free parameters in terms of the posterior-probability distribution marginalized over all other parameters, along with the marginal distributions of each free parameter. The colour scale is logarithmic, with each sub-plot separately normalized to its own maximum value; black indicates high probability and white low.

when $a_{\rm max}$ is very large. Even by increasing $a_{\rm max}$ by only one order of magnitude, the fit to the sub-mm data is dramatically improved, giving good agreement with the observed fluxes and spectral index. However, these models assume that the grain-size distribution is the same throughout the disc, with no consideration of grain settling or radial drift. As described in Section 3.1.2, we lack the observational constraints required to justify the complexity that this would add to our model, and must therefore accept that a larger dust mass is required to reproduce the observed (sub-)mm emission. However, the compact nature of the 1.3 mm emission provides a further hint that grain-growth and settling processes should be included in future models. Fig. 8 shows a simulation of the SMA observations computed using our best-fitting model as input to the SIMOBSERVE and SIMANALYZE tasks in CASA. As noted, the model does not reproduce the flux of the observations, being $\sim$ 2–3 times lower. However, the core of the emission of each disc appears more extended in the simulated image than the observation, suggesting a component of compact emission is missing from our model. A

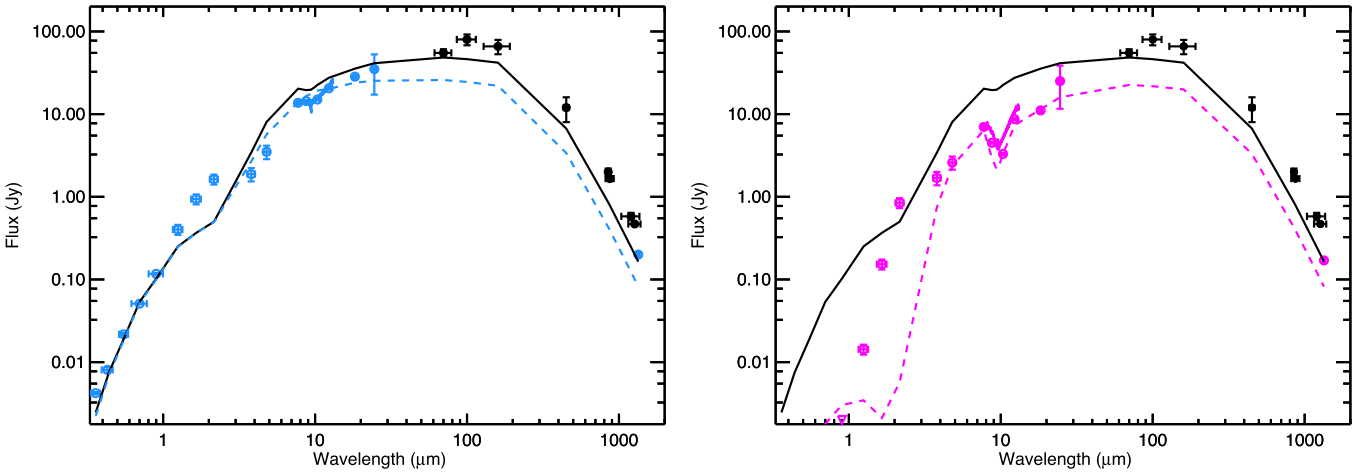

Figure 6. Simulated SEDs of the best-fitting model for the SW (left) and NE (right) components and the observed SEDs. In both cases, the solid black points correspond to photometry from observations which fail to resolve the two components of the binary (column Unres in Table 3), and the solid line corresponds to the sum of the model flux of both components. The coloured points correspond to resolved photometry, and the coloured dashed line indicates the best-fitting model's emission from each component separately. The triangle in the lower left of panel b indicates observed 3σ upper limit in *I* band; the upper limits at shorter wavelengths do not fit within the axes.

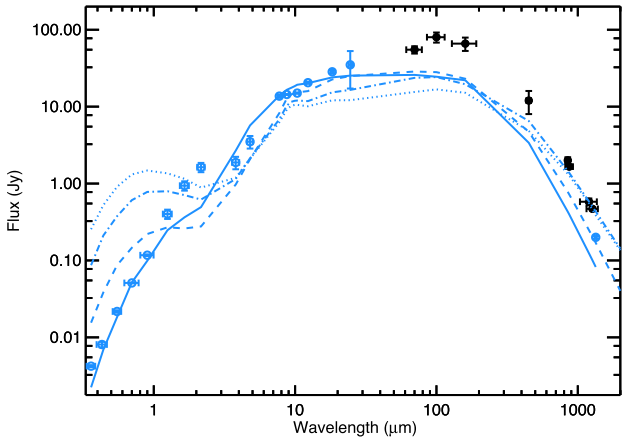

Figure 7. Influence of the maximum grain size on the SED of our best-fitting model for the SW component. As in Fig. 6, the blue points correspond to the resolved observations of the primary, and the black points to the unresolved photometry. The solid line shows the SED for VV CrA SW shown in Fig. 6 with small grains only, the dashed, dot–dashed and dotted lines extend the size distribution to 2.5, 25 and 250 μm, respectively. The 2.5 μm grains fit the sub-mm flux and spectral index well, without significantly perturbing the MIR–FIR fluxes.

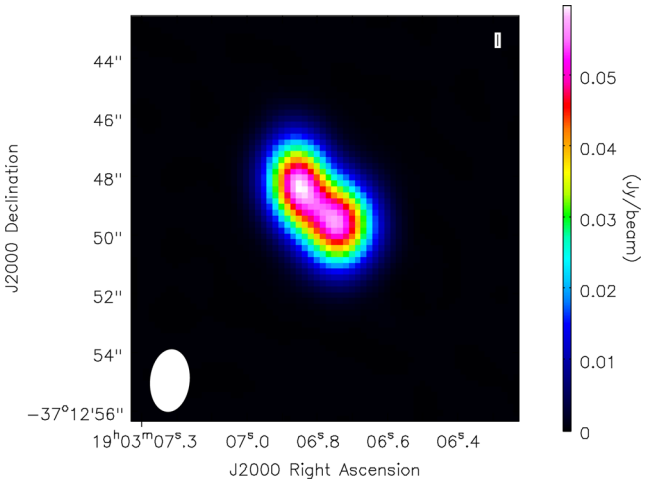

Figure 8. Simulated 1.3 mm image based on our best-fitting model. Produced using CASA SIMOBSERVE, neglecting all sources of noise other than UV-coverage. The total flux is underpredicted, but the discs are also too extended compared to Fig. 3

likely explanation is the lack of large dust grains in our model; these grains should rapidly settle to the mid-plane and experience radial drift, making them more centrally concentrated. As large grains are more efficient mm-wave emitters than the ISM grains in our model, this would result in an additional component of compact emission, which may dominate the SMA observations.

Fig. 9 and Appendix B compare the MIDI observations with the visibilities of our best-fitting model. In general, the model fits well, but tends to predict worsening resolution at longer wavelengths, in contrast to the observed visibilities, which tend to decrease with increasing wavelength. The emitting area of the disc as a function of wavelength must therefore increase faster compared to the size of the beam than our model assumes. One plausible explanation is an effect of the scattered flux; if ∼1 μm dust grains are present at the disc surface as implied by IR spectroscopy of sources in nearby star-forming regions (Furlan et al. 2006, 2009; Kessler-Silacci et al. 2006; McClure et al. 2010; Oliveira et al. 2010), these would efficiently scatter the radiation emitted by the disc, producing substantial additional extension. However, RT modelling of the optically thin case using MC3D suggests that the reduction in temperature of larger grains outweighs this effect, reducing the effective size of the disc. However, dust temperatures in real discs can be substantially different from the optically thin case, but this case is not feasible in the current version of MC3D. There is no evidence of emission from polycyclic aromatic hydrocarbons or stochastically heated grains, which would also introduce extended MIR emission. While it is possible that our model has converged on a solution with too little flaring, none of the observed visibilities show

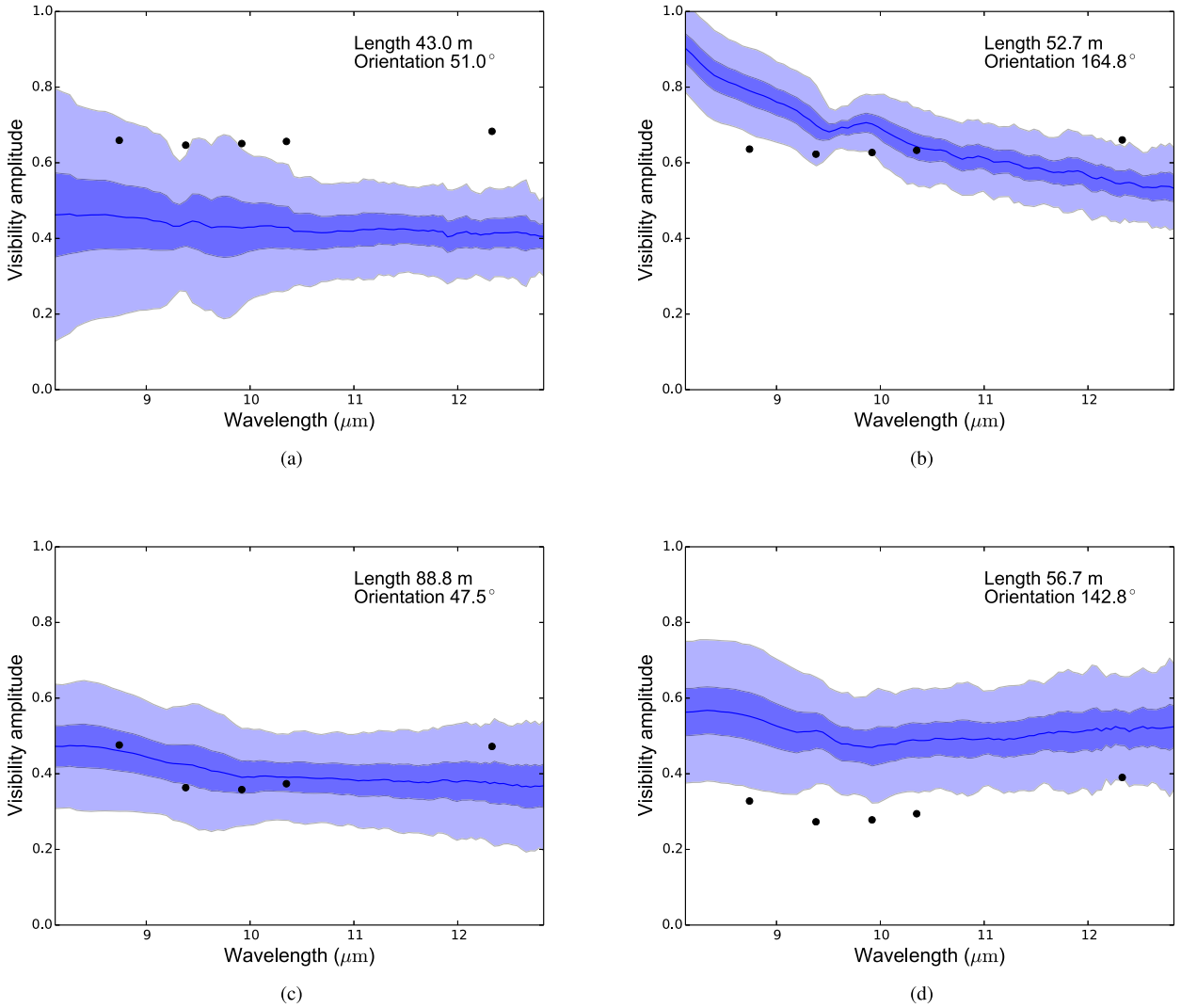

Figure 9. Comparison of two selected observed visibilities and their counterparts in our best-fitting model. *a* and b: observations of the primary. *c* and *d*: secondary component. The projected baseline length and orientation are given in the top-right corner of each plot. The full line indicates the observed visibility, the dark- and light-blue regions, respectively, indicate its 1σ and 3σ regions, and the black points the simulated visibilities.

the rise around 12 μm seen by van Boekel, Dullemond & Dominik (2005) for flared discs, arguing against this. Indeed, the observations are broadly consistent with their models for self-shadowed discs, suggesting that, rather than flaring, there may be additional structure missing from our model. The binary nature of the system makes structure a logical conclusion, as the discs would be subjected to perturbations by the companions; given the qualitative similarity to RW Aur (see e.g. Dai et al. 2015, and references therein), VV CrA may be an interacting binary at an earlier stage of evolution. However, we do not expect any signatures of interaction to be visible in existing data – any tidal tail would likely be lost in the missing flux in the SMA image, and the MIDI data lack the UV coverage required to detect spiral waves in the inner discs. These possibilities could plausibly be tested using the new generation of extreme adaptive optics (XAO) imagers (e.g. SPHERE) to acquire NIR imaging polarimetry, or by imaging the thermal emission at very high resolution for example with ALMA or the multi apeture mid-infrared spectroscopic experiment (MATISSE), discussed in further detail below.

Based on this tension between data and models, it is clear that future studies must consider more complex models of VV CrA. As noted above, there are suggestions of grain growth, decoupling between gas and dust, and additional structure in the discs. At present, it is not feasible to explore the full parameter space of these effects and their possible interactions with detailed radiative transfer models, and as noted above, existing data are unable to constrain such modelling, necessitating additional observational constraints. It is likely that models including such additional physics would produce a somewhat different best-fitting model than the simple parametrization used here. However, we expect this to have a larger effect on the disc mass, flaring index, and inclination angles, while the inner radius, low luminosity and foreground extinction should be relatively robust.

4.2 Mass and evolutionary state

We can determine an approximate stellar mass M and age t by comparing the temperature and luminosity of the best-fitting model to evolutionary tracks. Using the tracks of D'Antona & Mazzitelli (1997), we construct interpolating functions for $T_*(M,t)$ and $L_*(M,t)$ from the isochrones, which are then solved simultaneously for M and t. We thus determine a mass of 1.8 $M_\odot$ and an

age of 3.0 Myr; if the accretion luminosity determined in Section 2.2 is subtracted from the luminosity of the best-fitting model, we arrive at 1.7 $M_\odot$ and an age of 3.5 Myr. Similar estimates are found using other evolutionary models, for example Palla & Stahler (1999) and Siess, Dufour & Forestini (2000). These values are inconsistent with previous estimates which inferred a very young T Tauri system based on the shape of the SED in the MIR (e.g. Prato & Simon 1997), but approximately consistent with the model of Koresko, Herbst & Leinert (1997) for the primary. However, radiative-transfer-model fitting is only weakly sensitive to the stellar temperature, and relatively small variations imply significant changes in the mass and age. Only by improving spectral-type determinations can matters be improved.

Our best-fitting model implies a stellar radius of 2.4 $R_\odot$for the primary, which allows us to estimate an accretion rate from the accretion luminosity given in Section 2.2 as in Gullbring et al. (1998) and Schegerer et al. (2008). Assuming a mass of 1.7 $M_\odot$ as determined above and a truncation radius of 5 R_*, we derive an accretion rate of 4.0×10^{-8} $M_\odot$ yr^{-1}. This is similar to the values of $\dot{M}/M$ seen in spectroscopic surveys of nearby star-forming regions (e.g. Alcalá et al. 2014; Manara et al. 2016).

4.3 Outlook

As it is clear that a variety of questions remain concerning the state of VV CrA, we will now discuss which observations should be targeted to allow future modelling efforts to improve upon our limitations. As the major shortcoming of our models is the failure to consider larger dust grains, resolved observations in multiple ALMA bands should be considered a priority. Spatially resolved spectral-index maps of the two discs would allow a reasonable prescription of grain growth and settling to be incorporated in future models, giving more reasonable estimates of the dust masses. A by-product of such observations would be high-resolution spectral line data, allowing the disc inclinations and stellar masses of both components to be directly constrained. Knowing the masses of the stars would allow for a substantially improved age determination, while directly measured inclinations could conclusively differentiate between the two cases in Smith et al. (2009).

Another aspect that would considerably enhance modelling efforts would be robust knowledge of the spectral types of the stars and their accretion rates. To date, this has proven nearly impossible due to the near-complete veiling of the photospheric lines in the primary, and the lack of flux from the secondary. The most promising course of action seems to be deep, high-resolution NIR spectroscopy covering a large range of wavelengths, or perhaps combined optical-NIR spectroscopy from instruments like XSHOOTER; observations of this kind would maximize the chances of resolving weak photospheric lines. Combining such data with a fitting method as in Manara et al. (2013) would allow the incorporation of the effect of veiling, improving the chances of finding a suitable solution.

As noted above, it is likely that our model does not include sufficient structure to correctly describe the disc. Probing such structures on scales $\lesssim$ 10 au requires milliarcsec resolution, which is now possible thanks to extreme adaptive optics and interferometry. The new generation of planet-hunting imagers (e.g. SPHERE, GPI, SCExAO) provide precisely the high-resolution capabilities required in scattered light, while ALMA can achieve the same resolution in the sub-mm, where optical depths are much lower; these may also be able to detect larger scale structures, such as a circumbinary disc, envelope or tidal tail. Meanwhile, MATISSE will provide sufficient UV-coverage in the MIR to facilitate interferometric imaging in a reasonable amount of observing time, and will achieve a similar angular resolution to both ALMA and SPHERE, albeit with a much smaller field-of-view. Previous studies (Ruge et al. 2014) have shown that structures are rarely detectable at all wavelengths simultaneously, so the ability to cover a large wavelength range is critical.

5 CONCLUSIONS

We have conducted a detailed study of the enigmatic pre-main-sequence binary system VV CrA. New NIR spectroscopy of the primary has derived an accretion luminosity of 0.81 $\pm$ 0.07 $L_\odot$, and placed an upper limit on the extension of Br γ emission in the N–S direction of 10 mas. Archival SMA observations have been used to produce the first-resolved image of the binary at 1.3 mm, and MIR interferometry probes the inner regions of both discs.

Based on these observations and data from the literature, we have presented a model for VV CrA, showing that even a small misalignment of the discs is a plausible explanation for the differences between the two components of the binary, with inclinations of 50°–55°. The MIDI observations allow us to break the degeneracies inherent in SED fitting, improving the constraints on the mutual inclination. This model suggests a lower luminosity for the central stars than previous work, most likely a result of the variability of the IR companion. Based on our model, we infer an age of 3.5 Myr and stellar masses of 1.7 $M_\odot$; combining these results with the accretion luminosity yields an accretion rate of 4.0×10^{-8} $M_\odot$ yr^{-1}.

We also suggest observational priorities that may resolve outstanding questions. While resolved ALMA observations should be the priority to resolve disc structures and allow future models to include grain growth and settling, there is also a strong case for further NIR observations of both components. In particular, determination of at least two of mass, spectral type and luminosity for both components would provide a robust test of evolutionary models. Similar studies of other pre-main-sequence binaries should be conducted in order to build up a sample of coeval systems to constrain models of star and planet formation and evolution.

ACKNOWLEDGEMENTS

This work is based on observations made with ESO telescopes at the La Silla Paranal Observatory under programs 74.C-0209(A), 75.C-0014(A) and 91.C-0768(A). We would like to thank the anonymous referee for their comments, Casey Deen for performing the CRIRES observations and reading the manuscript, Chris Koresko for providing Keck/NIRC photometry, Hongchi Wang for helpful analysis of NACO photometry, and Peter Abraham for helpful discussions. This research was funded under Deutsche Forschungsgemeinschaft (DFG) programme nos. WO 857/10-1 and WO 857/13-1. CFM gratefully acknowledges an ESA Research Fellowship. The Submillimeter Array is a joint project between the Smithsonian Astrophysical Observatory and the Academia Sinica Institute of Astronomy and Astrophysics and is funded by the Smithsonian Institution and the Academia Sinica.

REFERENCES

Alcalá J. M. et al., 2014, A&A, 561, A2
Andrae R., 2010, preprint (arXiv:e-prints)
André P., Di Francesco J., Ward-Thompson D., Inutsuka S.-I., Pudritz R. E., Pineda J. E., 2014, in Beuther H., Klessen R. S., Dullemond C. P.,

Henning T., eds, Protostars and Planets VI. Univ. Arizona Press, Tucson, AZ, p. 27
Antoniucci S. et al., 2011, A&A, 534, A32
Appenzeller I., Jetter R., Jankovics I., 1986, A&AS, 64, 65
Briggs D. S., Schwab F. R., Sramek R. A., 1999, in Taylor G. B., Carilli C. L., Perley R. A., eds, ASP Conf. Ser. Vol. 180, Synthesis Imaging in Radio Astronomy II. Astron. Soc. Pac., San Francisco, p. 127
Calvet N., Muzerolle J., Briceño C., Hernández J., Hartmann L., Saucedo J. L., Gordon K. D., 2004, AJ, 128, 1294
Chelli A., Cruz-Gonzalez I., Reipurth B., 1995, A&AS, 114, 135
Chini R. et al., 2003, A&A, 409, 235
Cieza L. A. et al., 2009, ApJ, 696, L84
D'Antona F., Mazzitelli I., 1997, Mem. Soc. Astron. Ital., 68, 807
Daemgen S., Petr-Gotzens M. G., Correia S., Teixeira P. S., Brandner W., Kley W., Zinnecker H., 2013, A&A, 554, A43
Daemgen S., Elliot Meyer R., Jayawardhana R., Petr-Gotzens M. G., 2016, A&A, 586, A12
Dai F., Facchini S., Clarke C. J., Haworth T. J., 2015, MNRAS, 449, 1996
Doyle L. R. et al., 2011, Science, 333, 1602
Duchêne G., Kraus A., 2013, ARA&A, 51, 269
Dullemond C. P., Dominik C., 2004, A&A, 421, 1075
Furlan E. et al., 2006, ApJS, 165, 568
Furlan E. et al., 2009, ApJ, 703, 1964
Gräfe C., Wolf S., Guilloteau S., Dutrey A., Stapelfeldt K. R., Pontoppidan K. M., Sauter J., 2013, A&A, 553, A69
Gullbring E., Hartmann L., Briceño C., Calvet N., 1998, ApJ, 492, 323
Haniff C., 2007, New Astron. Rev., 51, 565
Henning T., Launhardt R., Steinacker J., Thamm E., 1994, A&A, 291, 546
Herczeg G. J., Hillenbrand L. A., 2014, ApJ, 786, 97
Hogg D. W., Bovy J., Lang D., 2010, preprint (arXiv:e-prints)
Jaffe W. J., 2004, in Traub W. A., ed., Proc. SPIE Vol. 5491, New Frontiers in Stellar Interferometry. SPIE, Bellingham, p. 715
Kaeufl H.-U. et al., 2004, in Moorwood A. F. M., Iye M., eds, Proc. SPIE Conf. Ser. Vol. 5492, Ground-based Instrumentation for Astronomy. SPIE, Bellingham, p. 1218
Kessler-Silacci J. et al., 2006, ApJ, 639, 275
Koresko C. D., Herbst T. M., Leinert C., 1997, ApJ, 480, 741
Kraus A. L., Hillenbrand L. A., 2009, ApJ, 704, 531
Kruger A. J., Richter M. J., Carr J. S., Najita J. R., Doppmann G. W., Seifahrt A., 2011, ApJ, 729, 145
Leinert C. et al., 2003a, Ap&SS, 286, 73
Leinert C. et al., 2003b, in Traub W. A., ed., Proc. SPIE Conf. Ser. Vol. 4838, Interferometry for Optical Astronomy II. SPIE, Bellingham, p. 893
Lodato G., Rice W. K. M., 2004, MNRAS, 351, 630
Lodato G., Rice W. K. M., 2005, MNRAS, 358, 1489
Lommen D. J. P. et al., 2010, A&A, 515, A77
McClure M. K. et al., 2010, ApJS, 188, 75
Madlener D., Wolf S., Dutrey A., Guilloteau S., 2012, A&A, 543, A81
Manara C. F., Beccari G., Da Rio N., De Marchi G., Natta A., Ricci L., Robberto M., Testi L., 2013, A&A, 558, A114
Manara C. F., Fedele D., Herczeg G. J., Teixeira P., 2016, A&A, 585, A136
Marraco H. G., Rydgren A. E., 1981, AJ, 86, 62
Mathis J. S., Rumpl W., Nordsieck K. H., 1977, ApJ, 217, 425
Mohanty S. et al., 2013, ApJ, 773, 168
Morel S. et al., 2004, in Traub W. A., ed., Proc. SPIE Conf. Ser. Vol. 5491, New Frontiers in Stellar Interferometry. SPIE, Bellingham, p. 1666
Muzerolle J., Hartmann L., Calvet N., 1998, AJ, 116, 2965
Neuhäuser R. et al., 2000, A&AS, 146, 323
Nutter D. J., Ward-Thompson D., André P., 2005, MNRAS, 357, 975
Oliveira I. et al., 2010, ApJ, 714, 778
Palla F., Stahler S. W., 1999, ApJ, 525, 772
Prato L., Simon M., 1997, ApJ, 474, 455
Prato L., Greene T. P., Simon M., 2003, ApJ, 584, 853
Przygodda F., 2004, PhD thesis, Max-Planck Institute of Astronomy, Heidelberg
Ratzka T., Leinert C., Przygodda F., Wolf S., 2008, in Richichi A., Delplancke F., Paresce F., Chelli A., eds, The Power of Optical/IR Interferometry: Recent Scientific Results and 2nd Generation Instrumentation, Springer-Verlag, Berlin, p. 519
Reipurth B., Zinnecker H., 1993, A&A, 278, 81
Roell T., Neuhäuser R., Seifahrt A., Mugrauer M., 2012, A&A, 542, A92
Rola C., Pelat D., 1994, A&A, 287, 676
Ruge J. P., Wolf S., Uribe A. L., Klahr H. H., 2014, A&A, 572, L2
Sanchez-Bermudez J., Hummel C. A., Tuthill P., Alberdi A., Schödel R., Lacour S., 2014, preprint (arXiv:e-prints)
Sauter J. et al., 2009, A&A, 505, 1167
Sault R. J., Teuben P. J., Wright M. C. H., 1995, in Shaw R. A., Payne H. E., Hayes J. J. E., eds, ASP Conf. Ser. Vol. 77, Astronomical Data Analysis Software and Systems IV. Astron. Soc. Pac., San Francisco, p. 433
Schegerer A. A., Wolf S., Ratzka T., Leinert C., 2008, A&A, 478, 779
Shakura N. I., Sunyaev R. A., 1973, A&A, 24, 337
Sicilia-Aguilar A., Henning T., Kainulainen J., Roccatagliata V., 2011, ApJ, 736, 137
Sicilia-Aguilar A., Henning T., Linz H., André P., Stutz A., Eiroa C., White G. J., 2013, A&A, 551, A34
Siess L., Dufour E., Forestini M., 2000, A&A, 358, 593
Smith R. L., Pontoppidan K. M., Young E. D., Morris M. R., van Dishoeck E. F., 2009, ApJ, 701, 163
Steenman H., The P. S., 1991, Ap&SS, 184, 9
Takami M., Bailey J., Chrysostomou A., 2003, A&A, 397, 675
Testi L. et al., 2014, in Beuther H., Klessen R. S., Dullemond C. P., Henning T., Protostars and Planets VI. Univ. Arizona Press, Tucson, AZ, p. 339
van Boekel R., Dullemond C. P., Dominik C., 2005, A&A, 441, 563
Weingartner J. C., Draine B. T., 2001, ApJ, 548, 296
Wilking B. A., Greene T. P., Lada C. J., Meyer M. R., Young E. T., 1992, ApJ, 397, 520
Williams J. P., Cieza L. A., 2011, ARA&A, 49, 67
Wolf S., 2003, Comput. Phys. Commun., 150, 99
Wolf S., Henning T., Stecklum B., 1999, A&A, 349, 839
Zinnecker H., 1984, Ap&SS, 99, 41

APPENDIX A: BAYESIAN INFERENCE

This discussion is based heavily on Hogg, Bovy & Lang (2010) and Andrae (2010), which the interested reader should peruse for a deeper understanding of the methods involved.

Suppose one has a set of data D which contains a number of observations, and wishes to identify which model M_i, drawn from a set of n models, fits these observations best. In a frequentist approach, one would seek to quantify the quality of the fit either by minimizing the χ^2 statistic or by maximizing the (logarithmic-) likelihood function $\mathcal{L} = P(D|M_i)$ i.e. by considering only how well the model reproduces the data set.

However, this does not account for any previous knowledge about the object being modelled, whether from statistical, theoretical, or literary considerations. Failing to include this information in the fitting process may lead one to prefer a model with slightly higher likelihood in spite of its intrinsically lower probability. To give an example appropriate to the main content of this article, consider a number of randomly oriented discs, where inclination $i = 0$ implies a face-on disc. For geometrical reasons, the probability of $\pi/3 \leq i \leq \pi/2$ is one half, and hence higher inclinations are intrinsically preferred. Therefore, if a low-inclination model has higher $\mathcal{L}$ in a particular case, the increased likelihood must outweigh the intrinsically lower probability of this configuration for the low-inclination model to be considered the better fit.

Such a priori information can be encoded as the distribution of the probabilities of the models $P(M_i)$ which is referred to as the *prior probability distribution* or more often simply the prior. Given

that what one wishes to calculate is the probability of model i given the observations or $P(M_i|D)$ (the *posterior*) one quickly arrives at

$$P\left(M_i|D\right) = \frac{P\left(D|M_i\right)P\left(M_i\right)}{P\left(D\right)}, \tag{A1}$$

which it can be clearly seen is Bayes theorem. Correct evaluation of the posterior therefore depends upon the correct choice of priors and likelihood functions, and their correct evaluation.

In the case of astronomical photometry, the statistical uncertainties are dominated by Poisson noise and are therefore nearly Gaussian, and the choice of likelihood function is straightforward. If observation d_j belongs to our data set D, and consists of a flux F_j observed at wavelength λ_j with associated photometric uncertainty $\sigma_{F,j}$ and bandwidth $\sigma_{\lambda,j}$ and the covariances are zero,[2] then provided that the modelled wavelengths agree with those observed the likelihood can be calculated from

$$\mathcal{L}_{ij} = \frac{\sigma_{F,j}\sigma_{\lambda,j}}{2\pi}\exp\left(\frac{-\sigma^2_{\lambda,j}}{2\sigma^2_{\lambda,j}\sigma^2_{F,j}}\left(F_j - F_{M_i,j}\right)^2\right), \tag{A2}$$

where $F_{M_i,j}$ and $\lambda_{M_i,j}$ are the wavelength and flux produced by model M_i that correspond with observation d_j.

Although the distribution of uncertainties for other astronomical observables are in general *not* Gaussian (e.g. Rola & Pelat 1994), in the absence of further information, the assumption of Gaussianity is no worse than any other. Hence, it is common to apply equation (A2) to all observables. For example, in the case of interferometric observations, the fluxes are replaced with the visibilities, and the bandwidth with the spectral resolution.

In the case of observables where two parameters must be fitted, equation (A2) must be altered slightly. For example, in the case of a polarimetric observation, where both the polarization fraction p and angle θ must be fitted, it becomes

$$\mathcal{L}_{ij} = \frac{\sigma_{p,j}\sigma_{\theta,j}}{2\pi}\exp\left(\frac{-1}{2\sigma^2_{\lambda,j}\sigma^2_{F,j}}\left(\sigma^2_{p,j}\left(p_j - p_{M_i,j}\right)^2 + \sigma^2_{\theta,j}\left(\theta_j - \theta_{M_i,j}\right)^2\right)\right). \tag{A3}$$

To find the likelihood of model i, one must then calculate the product $\mathcal{L}_i = \prod_j \mathcal{L}_{ij}$.

Once the posterior has been appropriately evaluated, the best fit can be extracted from the maximum of the distribution. However, one is usually more interested in the *credible interval* of each variable, usually taken as the 68.3 per cent credible region (or *1σ region*). This is the region within which 68.3 per cent of parameter estimates lie. To determine this, one must calculate the marginal distributions of the posteriors by integrating over all other variables i.e. for two variables a and b:

$$P(M_i|D,a) = \int_{b'} P(M_i|D,a,b)\,\mathrm{d}b', \tag{A4}$$

which leaves one with a 1D distribution of the posterior. From this, the 1σ region can be determined by integrating the distribution to find the region that contains 68.3 per cent of the probability. This region is non-unique, so it is common to define it either as the narrowest region, as a region symmetrical about the median, or one symmetrical about the mean. The results above refer to the narrowest region.

APPENDIX B: SIMULATED AND OBSERVED VISIBILITIES

Fig. B1 and B2 show the full set of observed MIDI visibilities and the simulated visibilities for our best-fitting model.

[2] In all likelihood, this is not a very good assumption, since the effective wavelength of a filter during an observation depends upon the spectral shape of the emission being observed.

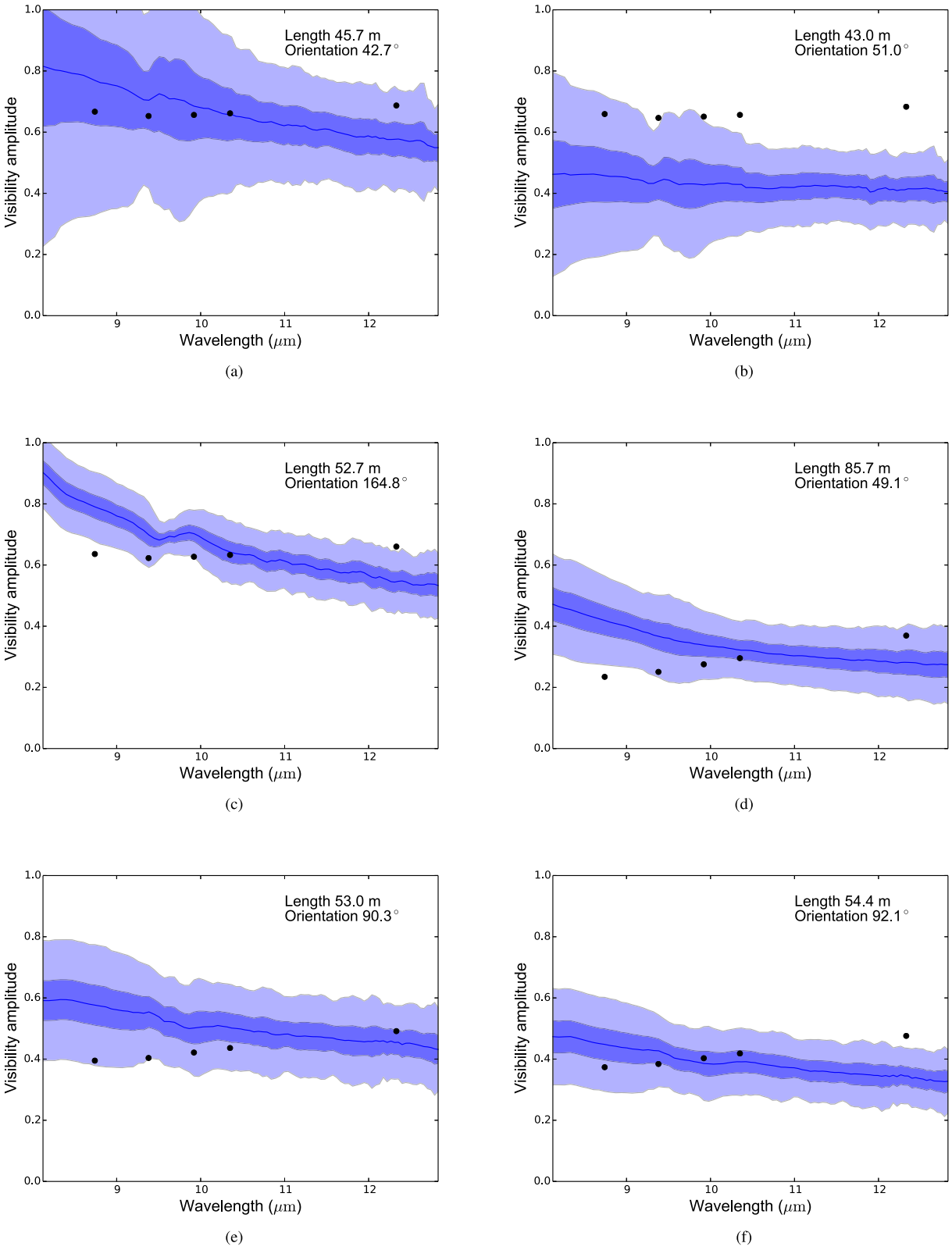

Figure B1. Comparison of observed visibilities and their counterparts in our best-fitting model as in Fig. 9 showing all observations for the primary.

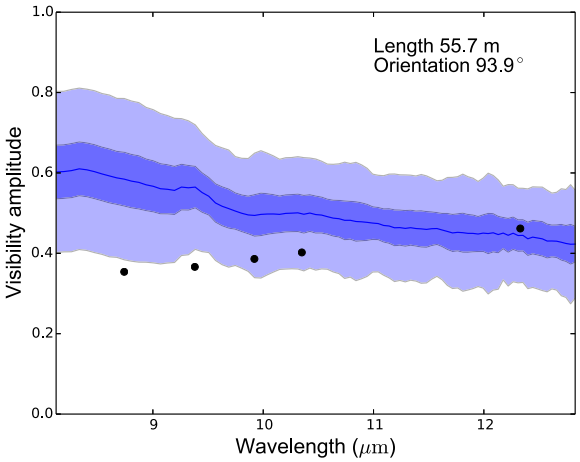

(a)

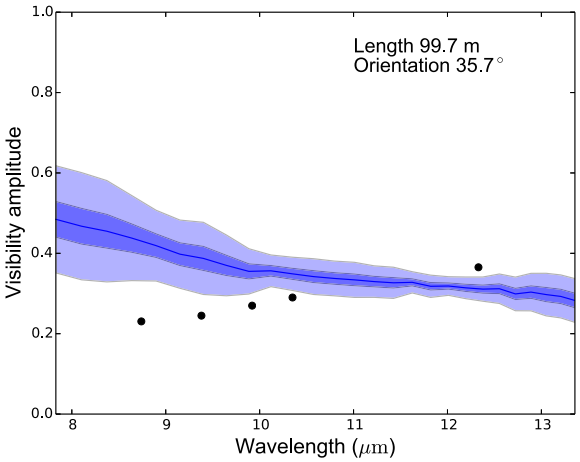

(b)

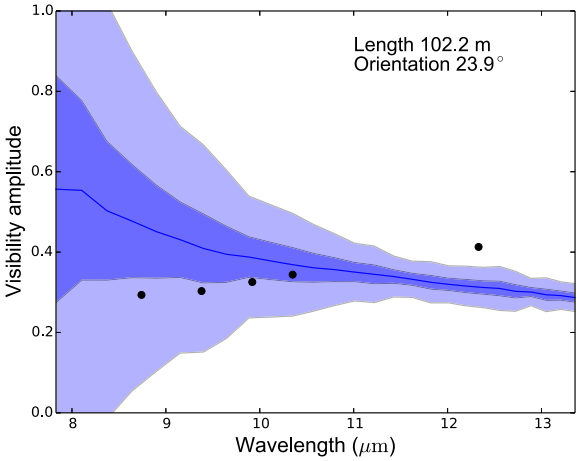

(c)

Figure B1 – *continued*

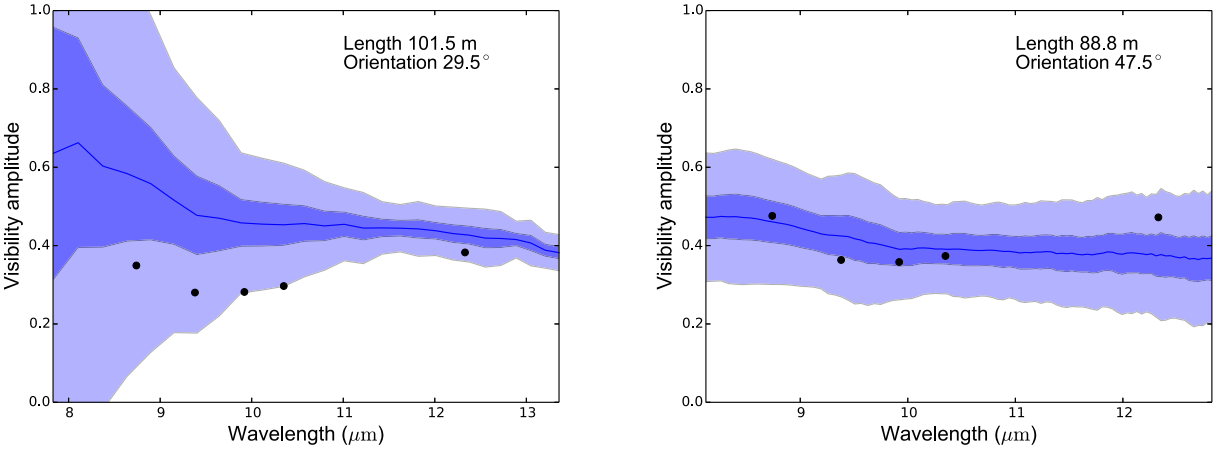

(a)

(b)

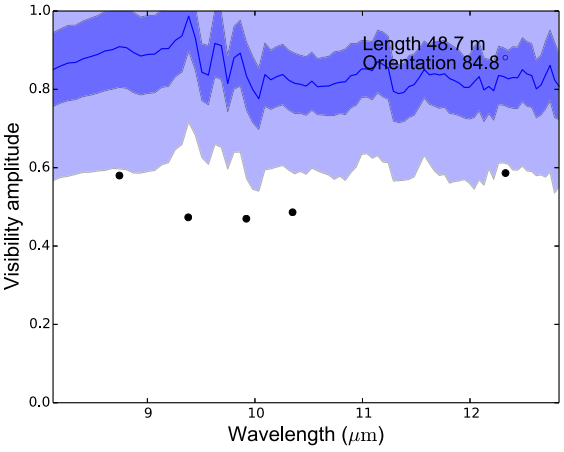

(c)

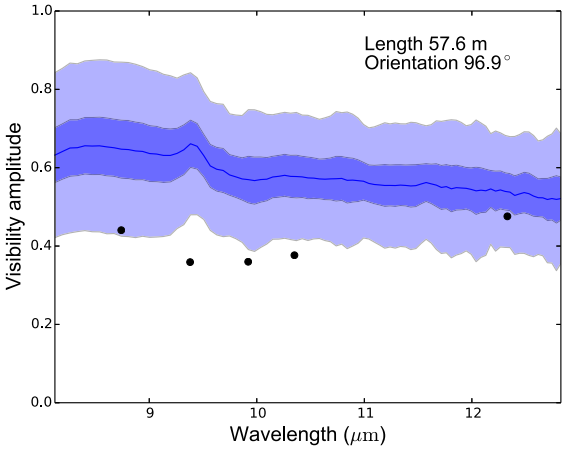

(d)

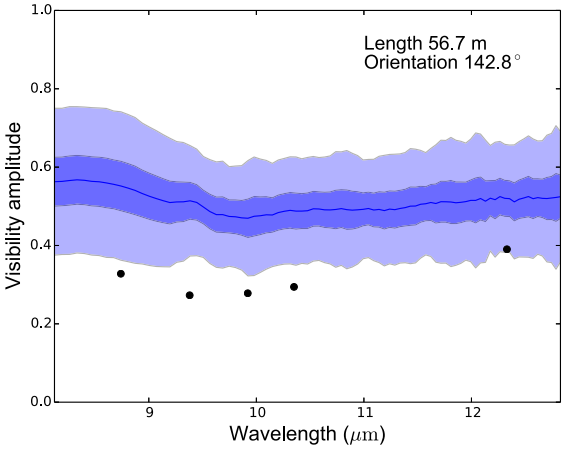

(e)

Figure B2. As Fig. B1, showing data for the secondary.

This paper has been typeset from a TEX/LATEX file prepared by the author.